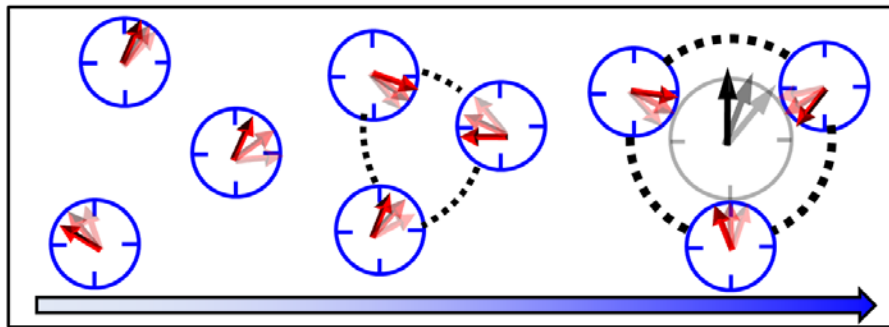
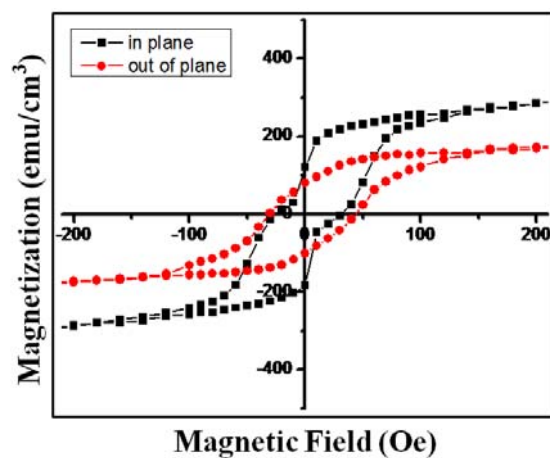


## **Part 1: Schematic illustration of the concept of synchronized self-assembly**

**Supplementary Figure 1**

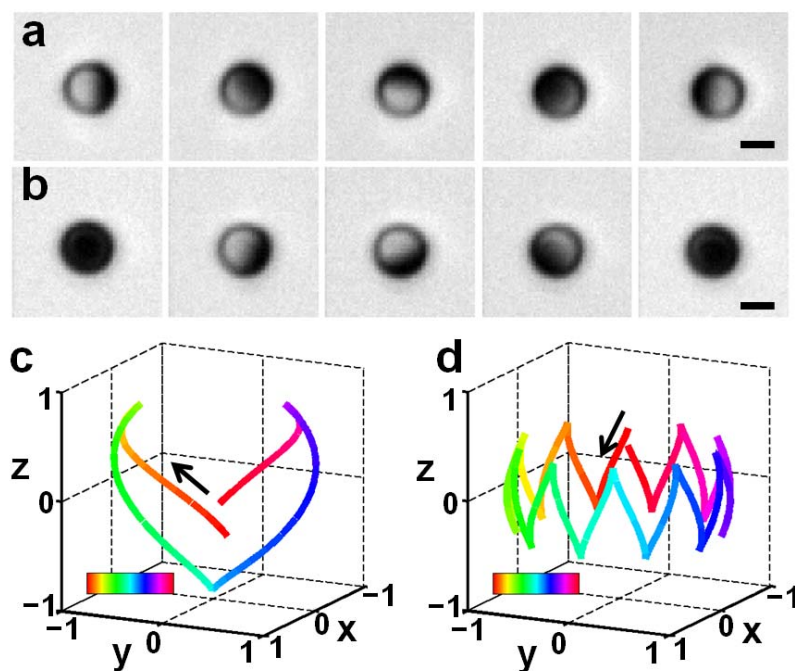


Schematic illustration of the concept of synchronized self-assembly. The red clock arrows represent phases of individual units undergoing periodic motion. The gradual paling of the arrows gives a sense of their dynamics and angular velocities. As units come closer and self-assemble (dotted lines represent interactions), their motions start to couple, as seen in the progressive approach towards frequency and phase locking. Finally, synchronization between the self-assembled structure and its constituent units limits steady-state self-assembly to specific synchronization-consistent structures.

**Part 2: Details of single-particle dynamics****Supplementary Figure 2**

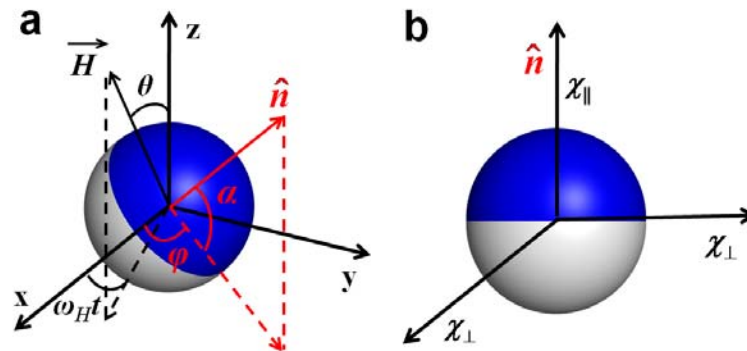
Magnetic hysteresis curve of an as-deposited nickel film (18 nm thick), deposited from above onto a dense monolayer of silica particles on a planar support. The magnetic parameters of individual colloidal particles are calculated from the areal density of the layer. The black curve is measured in the film plane. The red curve is measured in the direction perpendicular to the surface.

## Supplementary Figure 3



**(a,b)** Time-dependent optical microscope images of a single Janus particle in a precessing magnetic field at 20 Hz, field strength 5 mT and precession angle  $50^\circ$ . Images are spaced by 18 ms. Ni coating is 18 nm thick. Scale bars are  $2\ \mu\text{m}$ . The precession axis is perpendicular to the image (a) and horizontal in the image (b). **(c,d)** Time-dependent spatial three-dimensional trajectory following the tip of the Janus director, as predicted by the equations of motion for  $\theta = 50^\circ$  (c) and  $\theta = 25^\circ$  (d) for the same parameters as in (a). Here, time is coded using standard HSV color code, from 0 to 133 ms in (c) and from 0 to 534 ms in (d). The black arrows indicate the direction of time flow and the precession axis is parallel to the  $z$ -axis. The rotation speed slows with decreasing  $\theta$  while oscillation frequency in the orthogonal direction increases. The microscopy images are fully described by the equations of motion, as can be seen vividly in Supplementary Movies 1 and 2.

## Supplementary Figure 4



(a) Coordinates and symbols used in the derivation of the equations of motion. (b) Internal coordinates of an individual particle.

## Derivation of the equation of motion

This derivation follows the reasoning of Tierno *et al.*<sup>10</sup> We model the Janus particles as paramagnetic spheres with anisotropic magnetic susceptibility, shown in Supplementary Fig. 4b. We work at a field strength (5 mT) higher than the coercive field so that the response of the film is predominantly paramagnetic. Because only torque is involved in the single-particle dynamics, this dynamics is not influenced by the fact that the dipole moment is shifted from the geometric center. The volumetric magnetization is

$$\vec{m} = \chi \vec{H} = \chi_{\perp} \vec{H} - \Delta\chi (\vec{H} \cdot \hat{n}) \hat{n}$$

where  $\Delta\chi = \chi_{\perp} - \chi_{\parallel}$ . Here  $\chi_{\parallel}$  is the susceptibility parallel to  $\hat{n}$  and  $\chi_{\perp}$  the susceptibility in any direction perpendicular to  $\hat{n}$ . Only the second term, not collinear with  $\vec{H}$ , contributes to a torque on the particle  $\tau_m = \mu_w V_{Ni} \vec{m} \times \vec{H} = -\mu_w V_{Ni} \Delta\chi H^2 (\hat{n} \times \hat{H})(\hat{n} \cdot \hat{H})$ , where  $\mu_w$  is the permeability of water, the suspending liquid (close to the vacuum permeability  $\mu_0$ ), and  $V_{Ni}$  is the volume of nickel coated on one particle. We obtain  $\chi_{\perp}$  and  $\chi_{\parallel}$  by averaging the upper and lower branches of the hysteresis curve and applying a linear fit. We work at such low frequencies (10–100 Hz) that there is no lag in the magnetic response of the film to the external field.

The precessing magnetic field can be expressed as  $\vec{H} = H(\sin \theta \cos \omega_H t, \sin \theta \sin \omega_H t, \cos \theta)$ , where  $\omega_H$  is the frequency of the driving field. The particle's director can be expressed as  $\hat{n} = (\cos \alpha \cos \varphi, \cos \alpha \sin \varphi, \sin \alpha)$ , where  $\varphi$  is the azimuth angle and  $\alpha$  the complement of the inclination angle.

Under the conditions of the experiments, the hydrodynamic flow has a low Reynolds number ( $Re < 10^{-5}$ ) so that we can ignore inertia (i.e., the motion is overdamped). The extra weight due to the coating is less than 5% of the weight of the particle. This translates into a maximum

energy difference of about  $2 k_B T$  between downward-pointing and upward-pointing particles, far less than the magnetic energy of the particle itself, which is on the order of  $3 \times 10^4 k_B T$ . Hence, the weight of the coating has a negligible influence on particle orientation. Furthermore, since the magnetic energy is so much larger than  $k_B T$ , we do not include thermal noise in the derivation.

By balancing the viscous drag  $\tau_v$  against magnetic torque  $\tau_m$  we arrive at

$$0 = \tau_v + \tau_m = -\zeta_r \vec{\omega} + \mu_w V_{Ni} \vec{m} \times \vec{H}$$

where  $\zeta_r$  is the rotational drag coefficient of a sphere in the fluid, and  $\vec{\omega}$  is the particle's angular velocity. Here  $\zeta_r = 8\pi\eta R^3$ , where  $\eta$  is the solvent viscosity ( $8.9 \times 10^{-4}$  Pa·s for water at 293 K).

After some trigonometry we obtain

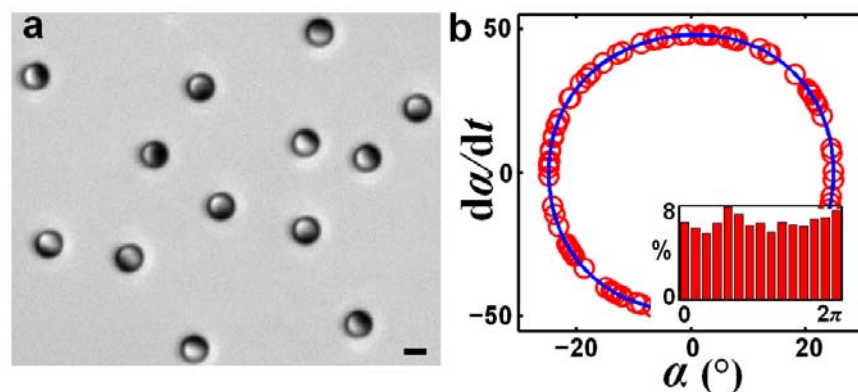
$$\frac{d\alpha}{dt} = \omega_c (\sin \alpha \cos \beta \sin \theta - \cos \alpha \cos \theta) (\cos \alpha \cos \beta \sin \theta + \sin \alpha \cos \theta)$$

$$\frac{d\beta}{dt} = \omega_H + \omega_c \frac{\sin \beta \sin \theta}{\cos \alpha} (\cos \alpha \cos \beta \sin \theta + \sin \alpha \cos \theta)$$

Here the parameter  $\beta = \omega_H t - \varphi$  is the phase lag between the azimuth angles of the external field and the particle, and  $\omega_c$  is defined as  $\mu_w V_{Ni} \Delta\chi H^2 / \zeta_r$ , a characteristic frequency arising when magnetic force and viscous force are balanced. We note that while a similar problem has been solved for rod-like particles<sup>10,31</sup>, the different sign of  $\Delta\chi$  leads to a completely different solution. For particles with rod-like magnetic symmetry, there exists a steady-state solution such that the particle precesses with the frequency of the external field and a precession angle smaller than  $\theta$ . However, for the present Janus particles with discoid magnetic symmetry, this mode is unstable. The equation set does not have a steady-state solution in which  $\alpha$  or  $\beta$  is constant. We solved this

equation set numerically in Matlab and obtained the trajectories of the director (Supplementary Fig. 3c and 3d provide two examples). The director oscillates between  $\theta$  and  $-\theta$ , while rotating around the precession axis with a lower frequency than the external field, the exact value of which depends on  $\theta$ .

### Supplementary Figure 5



**(a)** Optical microscope image of multiple particles sedimented to the bottom of the sample cell, under the influence of magnetic field with frequency 20 Hz and strength 5 mT, with precession axis perpendicular to the image. The precession angle  $\theta = 50^\circ$  was such that particles slightly repelled each other in the imaging plane to maintain separations large enough that coupling between their dynamics was negligible. Therefore they satisfied the free-particle condition of the simulations in panel b. The scale bar is 3  $\mu\text{m}$ . **(b)** Phase portrait of free particles generated by simulation. First,  $10^4$  particles were exposed to a static field in  $z$ , then to a precessing field with  $\theta = 25^\circ$ , mimicking the laboratory experimental procedure. The large blue circle, taken from the

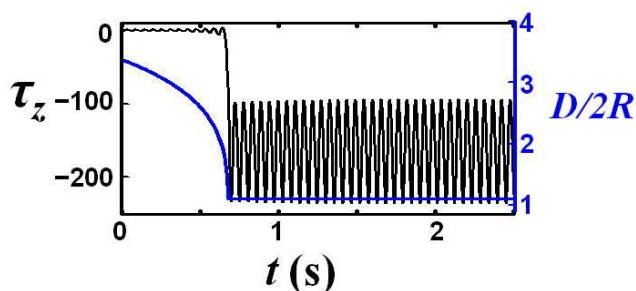
trajectory of one particle, shows the limit cycle of the dynamics in  $\alpha$ . Small red circles correspond to the instantaneous phase of 100 randomly picked particles; all of them fall on the limit cycle. The  $y$ -axis has units of rad/s. Inset shows a histogram of the distribution of all particles' instantaneous phases on the limit cycle.

### Discussion regarding the phase freedom

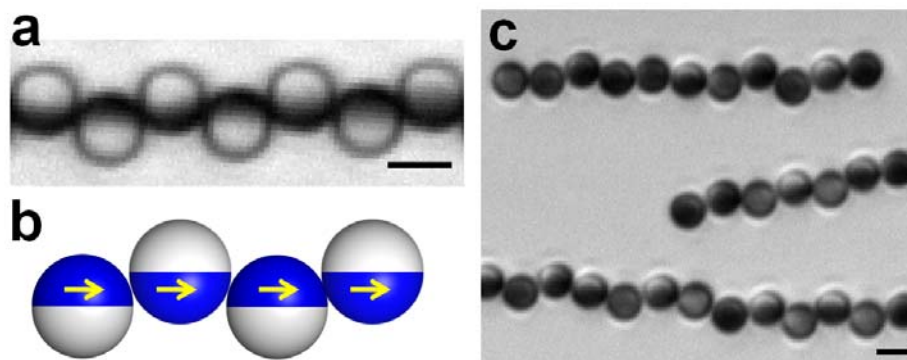
The dynamics of magnetic Janus particles in precessing fields exhibit generic properties of basic units capable of synchronization; first as self-sustained oscillators in  $\alpha$  (oscillation) and secondly as forced rotators in  $\varphi$  (rotation around the precession axis). Such dynamic systems are known to have a limit cycle with zero Lyapunov exponent in one direction and negative Lyapunov exponent in all other directions<sup>6</sup>. We confirmed this for the oscillatory motion by applying manual perturbations to steady-state trajectories (i.e., a limit cycle in the phase portrait  $d\alpha/dt$  versus  $\alpha$ , Supplementary Fig. 5b) in the numerical solution of the equations of motion. All perturbations away from the limit cycle relax back to the limit cycle, but perturbations along the limit cycle neither grow nor decay. The reason for the observed phase freedom is the degeneracy introduced by the discoid magnetic symmetry of magnetic Janus particles. Even in a static field that forces the director to remain in the plane perpendicular to the external field, particles can point in different degenerate directions within that plane.

### Part 3: Synchronization between two Janus particles

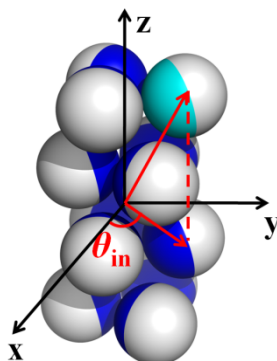
#### Supplementary Figure 6



Approach to synchronization of two particles in simulation. Time-dependent interparticle distance  $D$ , normalized by the particle diameter  $2R$  (right axis), and time-dependent torque  $\tau_z$  (in simulation units of N·m) are plotted against elapsed time. The two particles are initially separated by 3.5 diameters along the  $z$ -axis, which is the precession axis. Parameters are the same as for Fig. 1d in the main text. Physically, each particle's dipole moment generates a magnetic field that acts on the other particle's dipole. Their cross product torque adds to the torque provided by the external field but as the magnitude is significant only when particles are in close proximity, phase synchronization lags spatial approach. The sign of this additional torque is invariably negative, signifying that particles mutually slow one another, leading to lesser rotation frequency in the synchronized state. The oscillation in  $\tau_z$  reflects the continual oscillation of separation and relative orientation of the two dipoles, due to the nutation-like single-particle dynamics. In experiment, the final interparticle separation is determined by the balance between the magnetic attraction and electrostatic repulsion, which image analysis using home-written code<sup>32</sup> shows to be  $\sim 200$  nm. This is consistent with the Debye length of  $\sim 250$  nm, inferred from conductivity measurements made immediately before the experiment, following the standard procedure<sup>33</sup>. The Debye length does not decay over the time scale of the experiment ( $\sim 10$  min).

**Part 4: Zigzag chains****Supplementary Figure 7**

**(a)** Representative image of a zigzag chain in a horizontal static (5 mT) field. The result is similar to Ref 8. **(b)** Schematic representation of zigzag chains, with dipole moment of each sphere shown as a yellow arrow. The dipole moment is displaced from the geometric center due to the one-sided coating. **(c)** Representative discrete zigzag chains in Region II of the phase diagram (Fig. 2a in the main text). The field strength is 5 mT, with frequency 20 Hz and  $\theta = 30^\circ$ . Scale bars are 3  $\mu\text{m}$ .

**Part 5: Analysis of synchronization between the microtube and its constituent particles****Supplementary Figure 8**

Coordinate system for the quantitative assessment of tubular order. To quantify the positional

order in these tubular structures, we define  $S = \frac{1}{n} \left| \sum_{j=1}^n \exp(i2k\theta_{j\text{in}}) \right|$  where  $\theta_{j\text{in}}$  is the azimuth angle

of the position vector of particle  $j$  (cyan in the figure) and the sum runs over all particles in the tube. This definition yields  $S = 1$  for a perfect  $(kk0)$  structure and 0 for a random distribution around the  $z$ -axis.

**Derivation of the Adler equation for tubular structure of magnetic Janus particles**

Microtubes are driven to rotate by the rotation of their constituent particles. To derive the Adler equation, we do not consider out-of-plane nodding of the particles, fluctuations of their rotation velocity, or positional fluctuations, all of which are considered to be secondary effects. The analysis applies to a frequency range (10–100 Hz, experimentally) where particles do not have time to relax positionally. The orientation of a single particle, *in the reference frame of the tube*,

is quantified by the angle  $\psi$ , which we assume to be identical for each particle (an assumption confirmed by numerical simulations), and the energy  $E$  of a  $(kk0)$  structure is only a function of this angle. To proceed, we determine  $E(\psi)$  in Supplementary Fig. 9. As expected, the ground state of the tubular structure in a static or precessing field corresponds to a configuration with  $\psi = 0$ . Deviation from this configuration raises the energy due to less favorable dipole alignment, as characterized by  $dE/d\psi$ . Physically, this term means that a constituent particle in the reference frame of the tube experiences a torque  $\tau_p = -dE/d\psi$ , which drives the particle back to the lowest energy state,  $\psi = 0$ . A counter torque on the tube arises (normalized by the number of particles in the tube),  $\tau_{\text{tube}} = dE/d\psi$ . This torque provides the driving force for rotation of the entire structure.

From a force analysis we find that  $dE/d\psi = \varepsilon \sin\psi$ , and numerical calculation of  $dE/d\psi$  (Supplementary Fig. 9a) confirms this sinusoidal dependence. The coupling coefficient  $\varepsilon$  quantifies the “rigidity” of the structure in response to distortion.

By definition,  $d\psi/dt = \omega - \Omega$  where  $\omega$  is the angular velocity of a constituent particle and  $\Omega$  the angular velocity of the entire tube, *in the laboratory reference frame*. Here we derive these two terms, in order to obtain  $d\psi/dt$ .

By balancing the magnetic torque on the tube by the viscous drag of the entire structure, we find

$$\Omega = \frac{\varepsilon}{\zeta_{\text{tube}}} \sin\psi, \text{ where } \zeta_{\text{tube}} \text{ is the rotational frictional coefficient of the tube in the fluid.}$$

Next, we derive  $\omega$ . In addition to  $\tau_p$  derived arising from interparticle interactions, each constituent particle also experiences a magnetic torque from the external field. We approximate this torque as  $\zeta_r \omega_{\text{free}}$ , which is the magnitude needed to balance viscous drag if the particle were a

free particle rotating with the averaged angular velocity  $\omega_{\text{free}}$  predicted by the single-particle equations of motion, at the specified  $\theta$ . One can understand  $\omega_{\text{free}}$  as the inherent frequency of the particle, before it is coupled to the microtube. Thus, the total magnetic torque  $\tau_{\text{mag}}$  on a constituent particle is  $\tau_{\text{mag}} = \zeta_r \omega_{\text{free}} - \varepsilon \sin \psi$ . Balancing  $\tau_{\text{mag}}$  with viscous drag  $\zeta_r \omega$ , we obtain the particle's angular velocity  $\omega = \omega_{\text{free}} - \frac{\varepsilon}{\zeta_r} \sin \psi$ . Notice that the second term slows the single-particle rotation for  $\psi < \pi/2$ . Equation (1) in the main text then follows from combining the definition of  $\psi$  with the above analysis,

$$\frac{d\psi}{dt} = \omega - \Omega = \omega_{\text{free}} - \varepsilon(\zeta_r^{-1} + \zeta_{\text{tube}}^{-1}) \sin \psi$$

which has the same form as the Adler equation for synchronization<sup>20</sup>. For  $\omega_{\text{free}} < \omega_{\text{c-free}} = \varepsilon(\zeta_r^{-1} + \zeta_{\text{tube}}^{-1})$ , this equation has a steady-state solution, in which  $d\psi/dt = 0$  and

$\psi = \arcsin \frac{\omega_{\text{free}}}{\varepsilon(\zeta_r^{-1} + \zeta_{\text{tube}}^{-1})}$ . Then, when synchronized, the rotation speed of the tube and its

constituent particles equal  $\Omega = \omega = \frac{\omega_{\text{free}}}{\zeta_{\text{tube}} / \zeta_r + 1}$ .

Thus, when the particles and the tube are synchronized, the ratio  $\omega_{\text{free}}/\omega$  is a constant independent of  $\varepsilon$  and  $\omega$ , and always greater than 2 since  $\zeta_{\text{tube}} > \zeta_r$ . Our simulations confirm this relation. Moreover, the higher  $k$  for a structure, the more slowly it rotates in the same magnetic field, due to the larger  $\zeta_{\text{tube}}$ . While the magnitude of  $\zeta_{\text{tube}}$  is difficult to calculate in a full hydrodynamic analysis, we can approximate it as the sum of the drag on each particle independently,  $6\pi\eta R R_{\text{tube}}^2$ , where  $R_{\text{tube}}$  is the tube radius. With this simplification, we find

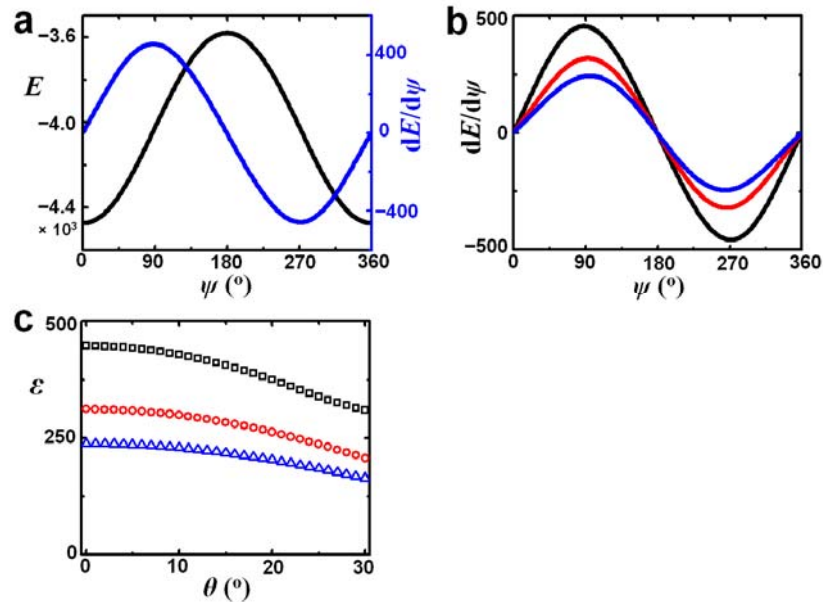
$\zeta_{\text{tube}}/\zeta_r = 1.45, 2.18$  and  $3.20$  for  $k = 3, 4, 5$ , respectively, close to  $\zeta_{\text{tube}}/\zeta_r$  value obtained in our simulations ( $1.88, 2.64$  and  $3.47$ , for (330), (440) and (550), respectively).

Rotation of one particle also creates a hydrodynamic shear flow and exerts a force on neighboring particles; this force also contributes to the torque on the whole tube. However, estimation shows that hydrodynamic interactions are a secondary effect, too weak to cause synchronization between the tube and constituent particles unless the separation is unrealistically small ( $\sim 2$  nm), far less than the  $200$  nm that we measure experimentally. Specifically: following the approach of Ref. 34, consider two spheres of radius  $R$  ( $1.5 \mu\text{m}$ ) that rotate with rotational frequency  $\omega$  around their respective centers while simultaneously rotating with rotational frequency  $\Omega$  as a pair (surface separation  $d$ ) around the center of their common axis. In the absence of magnetic coupling between the spheres, the drag force on each sphere must be balanced by a lateral force on the same sphere generated by the hydrodynamic coupling,

$$-0.1 \ln(d/2R) \zeta_r \omega / R = 6\pi\eta R \Omega (d/2 + R)$$

The experimentally observed separation  $d = 200$  nm yields  $\Omega/\omega \sim 0.36$ . This is less than what is required for synchronization,  $\Omega/\omega = 1$ . The hydrodynamic contributions could, if needed, be included in the Adler equation as a simple additive term.

## Supplementary Figure 9

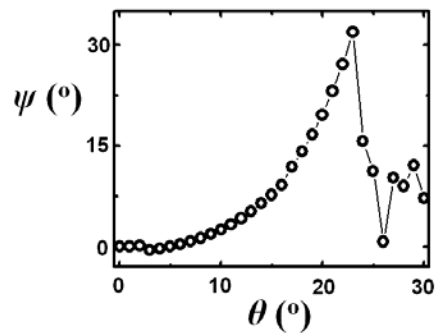


Calculation of the energy  $E$  per particle for various microtubule structures.  $E$  is reported in the reduced unit of energy  $k_B T$  (defined in Part 7), and  $dE/d\psi$  and  $\varepsilon$  are expressed in  $k_B T/\text{rad}$ .  $E$  varies negligibly with the in-plane angle of the external magnetic field, due to the symmetry of  $(kk0)$  structures.  $dE/d\psi$  is calculated via a uniform perturbation in  $\psi$  applied to all particles simultaneously. For simplicity, only interactions between particles are included, since the interaction of the particle moment with the external field does not change with  $\psi$ , the second-order effect in which the external field acts on enhanced magnetic moments is not included. Magnetic parameters are selected to compare with the distributions in Fig. 2c in the main text; they match a nickel coating of 21 nm thickness. **(a)** In a static ( $\theta = 0^\circ$ ) magnetic field of 5 mT along the  $z$ -axis,  $E$  (black) and  $dE/d\psi$  (blue) are plotted versus  $\psi$  for the (330) structure.  $dE/d\psi$  varies sinusoidally with  $\psi$ . From the maximum of the  $dE/d\psi$  curve,  $\varepsilon$  is extracted. **(b)** In a static

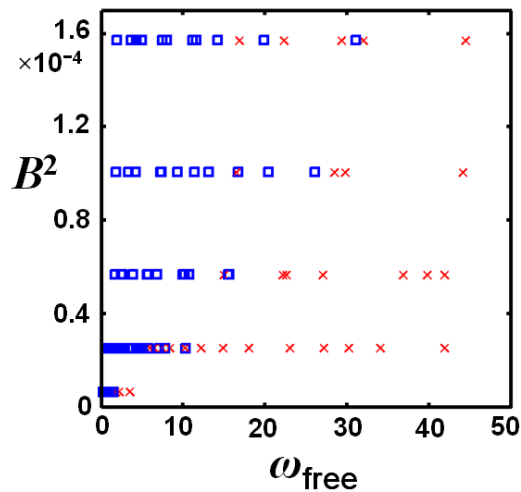
magnetic field of 5 mT along the  $z$ -axis,  $dE/d\psi$  is plotted versus  $\psi$  for different structures: black, (330); red, (440); blue, (550). The same color coding applies to panel c. In a static field, the energy per particle for (330), (440) and (550) is  $-42173$ ,  $-42304$  and  $-42353 k_B T$ , respectively.

(c) Coupling parameter  $\varepsilon$  plotted against  $\theta$  for different structures.  $\varepsilon$  varies weakly with  $\theta$ .

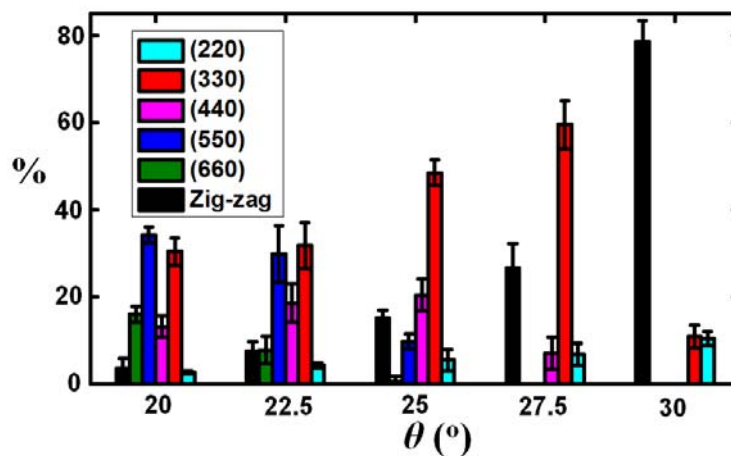
### Supplementary Figure 10



$\psi$  plotted against  $\theta$  in simulated (330) tube with parameters corresponding to a 21 nm Ni coating. Though the Adler equation mathematically defines a transition at  $\psi = \pi/2$ , the microtube might not be able to sustain such a large distortion. In simulation the transition appears to begin at  $\psi \approx 30^\circ$ , when the particle directors start to point to their neighbors instead of the center. At this time the structure becomes looser, which decreases the effective coupling coefficient  $\varepsilon$ , triggering the actual synchronization transition. Then phase slip sets in and the structure dissociates via the pathway described in Fig. 3c in the main text. With the derived value of  $\varepsilon$  and assuming  $\psi_c = 30^\circ$ , the Adler equation predicts  $\theta_c$  ( $24^\circ$ ) very close to this observed transition.

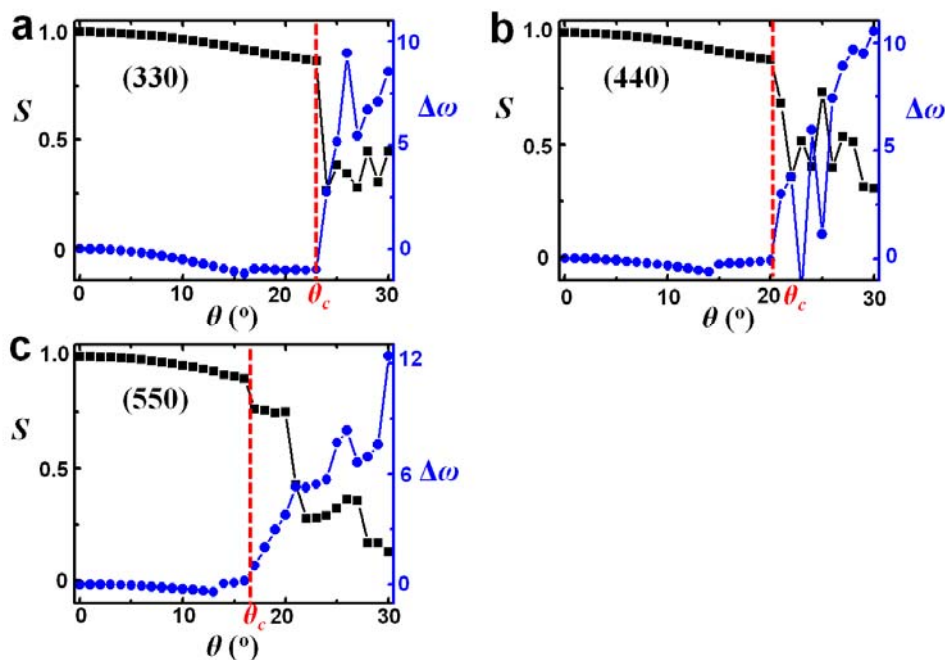
**Supplementary Figure 11**


The experimentally measured state diagram, Fig. 2a of the main text, is replotted in the  $B^2-\omega_{\text{free}}$  plane, to compare with the classic  $\varepsilon-\nu$  plot in synchronization<sup>6</sup>. Here  $B$  is the strength of the magnetic field in tesla and  $\omega_{\text{free}}$  the single particle rotation frequency (rad/s), calculated from the equations of motion. Only the portion concerning the synchronization transition is shown. The blue squares denote the region inhabited by microtubes and red crosses denote the region consisting purely of zigzag chains. This plot essentially gives the right half of the Arnold tongue known in the field of synchronization<sup>6</sup>. Though the data exhibit scatter, this plot does show a roughly linear boundary between the region of microtube and the zigzag chain, as predicted from the Adler analysis. The effect of external frequency enters indirectly through the modulation of  $\omega_{\text{free}}$ , as quantitatively described by the equations of motion in Part 2.

**Part 6: Selection of tubular structures****Supplementary Figure 12**

Experimentally determined distributions of microtube structures are plotted against  $\theta$ , showing all  $(kk0)$  structures that we observed at a given  $\theta$ . The  $(220)$  and  $(660)$  structures contribute less than 15% under all conditions tested. An abbreviated version of these distributions is given in Fig. 2c in the main text. Many higher- $k$  structures coexist below  $20^{\circ}$ , but their visual identification is difficult.

## Supplementary Figure 13



Limits of stability of various microtubes, obtained by simulating particles with 21 nm nickel coatings. The order parameter  $S$  and the frequency difference  $\Delta\omega$  (units of rad/s) are plotted against  $\theta$  for different microtubes. Before reaching the instability transition, the small negative trends reflect end effects; a visual check confirms that the main structures are phase-locked and stable. Above  $\theta_c$  the plots are noisy, because the microtubes have lost synchronization and have disassembled into loose aggregates whose overall rotation speeds are ill-defined. The simulated critical values of  $\theta_c$ ,  $23^\circ$ ,  $20^\circ$  and  $16^\circ$  for (330), (440) and (550) structures, respectively, agree in trend with experimental observations but are slightly lower quantitatively, probably due to the point dipole simplification or omission of hydrodynamic interactions.

## **Part 7: Simulation details**

Simulations are performed via molecular dynamics including self-consistent magnetic interactions and shifted-truncated Lennard Jones (STLJ) interactions; both aspects are described below. Simulations are performed using reduced units. The particle diameter is taken to be 4.3 in simulation length units, equivalent to a physical diameter of 3  $\mu\text{m}$ , and the fluid density is taken to be 2.5 in simulation density units, corresponding approximately to the density of water at room temperature. The simulated particles are neutrally buoyant, as experiments confirm buoyancy and substrate interaction do not significantly affect the observed phenomena. All simulations are performed at field strength and frequency equivalent to 5 mT and 20 Hz, for  $2 \times 10^8$  timesteps, long enough to conclusively determine the steady-state behavior.

We take the Boltzmann constant  $k_B = 1$  and the temperature  $T = 1$ , giving an energy or equivalently a time conversion between experiment and simulation units. However, thermal effects are not incorporated in the simulation. We take the permeability of free space  $\mu_0 = 1$  giving a conversion between laboratory and simulation magnetic units.

The system size is  $40 \times 40 \times 80$  or  $40 \times 40 \times 160$  with up to 80 particles in a microtube. Whereas the simulation cell has periodic boundary conditions, the tubes are finite and aligned with the long side of the cell. The system is large enough to prevent either periodicity artifacts or dominant end effects. Doubling the number of particles (i.e., doubling the length of the microtubes) did not lead to qualitative changes. In addition, we note that because for isolated tubes this is effectively a one-dimensional problem, the  $1/r^3$  nature of the dipolar interaction does not lead to a divergence of the total energy.

The time step is 0.001 ( $= 1.26 \times 10^{-7}$  s), which gives sufficient energy stability in the overdamped regime where we operate. The need to simulate accurately in the overdamped regime—for example to reproduce the crossover between a particle following the field and the higher-frequency regime where the field-induced torque cannot balance viscous drag—produces the largest constraint on coarse graining our simulation for computational efficiency. To be conservative, our parameters almost exactly match physical values in experiment, after unit conversions.

The interactions in the simulation are translational and rotational Langevin damping of each particle and the magnetic and STLJ interactions between particles. The Langevin dynamics are at zero temperature and operate on each particle separately. As mentioned in the derivation of the equations of motion, the disregard of thermal effects is justified by the fact that the strength of interaction ( $\sim 10^4 k_B T$ ) greatly exceeds the thermal energy. The drag coefficients are those of a sphere in water.

Each particle is treated as a point dipole shifted slightly from the particle's geometric center, selecting the dipole shift such that a single chain in static magnetic field assembles with a zigzag angle<sup>8</sup> close to observed experimental values. For example, when the laboratory nickel coating is 18 nm thick, the dipole shift is 0.240 simulation length units away from the particle's geometric center; for a 21 nm coating, the corresponding simulation value is 0.213. The magnetic susceptibility is scaled by the coating thickness.

At each time step, magnetic interactions are re-evaluated by solving the linear system of equations for each particle's magnetic moment as a function of the field produced by the other

particles and the spatially uniform, time-dependent external field. For each of the  $n$  particles, there is an equation for the magnetic moment  $\vec{m}_i$ ,

$$\vec{m}_i = \chi \vec{H}_{\text{total}} = \chi(\vec{H}_{j \neq i} + \vec{H})$$

where  $\chi$  is the anisotropic magnetic susceptibility tensor and  $\vec{H}_{j \neq i}$  is the magnetic field produced by all other particles, which is a linear function of the magnetic moments  $\vec{m}_j$  for  $j \neq i$ <sup>35</sup>. For example, for the 18 nm nickel coating studied in the laboratory, in simulation units  $\chi_{\perp} = 21.870$  and  $\Delta\chi = 10.619$ .

Once the magnetic moments are determined, calculation of forces and torques on each particle is straightforward. The minimum-image convention is used, so forces do not operate at more than 20 length units. The STLJ interactions employ  $\varepsilon = 2500$ , which is sufficiently large to prevent the particles approaching within the singularity in magnetic susceptibility, and  $\sigma = 4.3$ , with the usual cutoff at  $2^{1/6} \sigma$  and a shift such that the potential is smooth at the cutoff. We verified that the general conclusions are independent of the detailed form of the repulsive term.

Simulations to evaluate tubular structure stability begin with particles arranged in the given tubular structure, at the equilibrium average pair distance, with particles oriented toward the central axis of the tube.

## References

31. Coq, N., Ngo, S., du Roure, O., Fermigier, M. & Bartolo, D. Three-dimensional beating of magnetic microrods. *Phys. Rev. E* **82**, 041503 (2010).
32. Anthony, S. M., Kim, M. & Granick, S. Single-particle tracking of Janus colloids in close proximity. *Langmuir* **24**, 6557-6561 (2008).
33. Sharma, V., Yan, Q., Wong, C. C., Carter, W. C. & Chiang, Y.-M. Controlled and rapid ordering of oppositely charged colloidal particles. *J. Colloid Interface Sci.* **333**, 230-236 (2009).
34. Drescher, K. *et al.* Dancing *Volvox*: hydrodynamic bound states of swimming algae. *Phys. Rev. Lett.* **102**, 168101 (2009).
35. Biswal, S. L. & Gast, A. P. Rotational dynamics of semiflexible paramagnetic particle chains. *Phys. Rev. E* **69**, 041406 (2004).